



# Photocatalytic H<sub>2</sub> production from aqueous methanol solutions using metal-co-catalysed Zn<sub>2</sub>SnO<sub>4</sub> nanostructures



Julio Núñez<sup>a</sup>, Fernando Fresno<sup>b</sup>, Laura Collado<sup>a</sup>, Prabhas Jana<sup>a</sup>, Juan M. Coronado<sup>a</sup>, David P. Serrano<sup>a,c</sup>, Víctor A. de la Peña O'Shea<sup>b,\*</sup>

<sup>a</sup> Thermochemical Processes Unit, IMDEA Energy Institute, Móstoles Technology Park, Avenida Ramón de la Sagra 3, 28935 Móstoles, Madrid, Spain

<sup>b</sup> Photoactivated Processes Unit, IMDEA Energy Institute, Móstoles Technology Park, Avenida Ramón de la Sagra 3, 28935 Móstoles, Madrid, Spain

<sup>c</sup> Chemical and Environmental Engineering Group, ESCET, Rey Juan Carlos University, c/Tulipán s/n, 28933 Móstoles, Madrid, Spain

## ARTICLE INFO

### Article history:

Received 29 December 2015

Received in revised form 4 March 2016

Accepted 9 March 2016

Available online 11 March 2016

### Keywords:

Photocatalytic H<sub>2</sub> production

ZnSn<sub>2</sub>O<sub>4</sub>

Co-catalyst

Pt

Au

## ABSTRACT

The activity of nanocrystalline Zn<sub>2</sub>SnO<sub>4</sub> for photocatalytic hydrogen production from methanol aqueous solutions has been explored. A co-precipitation method starting from metal salts and a mild base as precipitating agent was used to obtain highly crystalline nanosized Zn<sub>2</sub>SnO<sub>4</sub> with cubic inverse spinel structure. In-situ photodeposition of Pt and Au nanoparticles as co-catalysts was performed prior to the photocatalytic reaction. The obtained materials have been characterised by XRD, TEM, N<sub>2</sub> adsorption isotherms and ICP-OES, Raman, UV-vis and photoluminescence spectroscopies. Bare Zn<sub>2</sub>SnO<sub>4</sub> gives rise to hydrogen release from a methanol aqueous solution without catalyst deactivation. This photocatalytic activity is remarkably increased with the deposition of platinum. In contrast, the use of gold as co-catalyst increases the activity only slightly, with a lower hydrogen production than a Pt-loaded sample with the same nominal metal content. An improved charge separation and the activity of Pt as hydrogen evolution catalyst are invoked to account for the present findings.

© 2016 Elsevier B.V. All rights reserved.

## 1. Introduction

Photocatalytic hydrogen generation from water or from alcohol aqueous solutions represents a very promising alternative to the current pathways to H<sub>2</sub> due to three main reasons: (1) It can be based on a renewable energy source provided that solar or renewable artificial irradiation is used; (2) it allows dealing with the intermittent character and seasonal variation of renewable energy sources by storing energy in the form of H<sub>2</sub>; and (3) it is an environmentally safe technology without pollutant by-products. However, there are still remarkable challenges to overcome, especially those related to the requirements of an ideal photocatalyst (chemical stability, sunlight harvesting, suitable band edges, limited recombination) that would allow a feasible and reliable H<sub>2</sub> production in both economic and technological terms. Accordingly, remarkable efforts have been undertaken in order to develop an efficient photocatalyst for H<sub>2</sub> production. In particular, although a number of semiconductor materials prepared as nanostructured photocatalysts have demonstrated to be effective in this reaction [1–5],

catalysts based on ZnO may be an appropriate selection because this is an environmentally friendly material with relatively high photoactivity, although it may not be suitable in certain conditions due to the possibility of photocorrosion [3]. To further improve the photoactivity of ZnO, several studies focusing on physicochemical modifications and on synergies with other materials have been carried out [6–8]. Another approach to improve the optical properties and the photoactivity of ZnO is the substitution of Zn<sup>2+</sup> ions by other cations with higher valence such as In<sup>3+</sup>, Al<sup>3+</sup> and Ga<sup>3+</sup> that can act as efficient shallow donors [9]. Indeed, Maeda et al. [10] have reported a record photocatalytic performance by means of this kind of modifications, reaching a H<sub>2</sub> yield of 240 μmol/h<sup>−1</sup> with a Rh-Cr/(Ga<sub>1−x</sub>Zn<sub>x</sub>)(N<sub>1−x</sub>O<sub>x</sub>) photocatalyst under visible light illumination.

Chemically related to ZnO, zinc stannate (Zn<sub>2</sub>SnO<sub>4</sub> or ZTO) has attracted considerable interest due to its intrinsic optical and electrical properties, such as high electron mobility (10<sup>−15</sup> cm<sup>2</sup> v<sup>−1</sup> s<sup>−1</sup>), high electrical conductivity (10<sup>4</sup> S cm<sup>−1</sup>), and adequate band structure (BG ≈ 3.4 eV) for photocatalytic reactions. This material has been widely explored as gas sensor, working electrode in dye-sensitized solar cells, photoluminescent material and as photocatalyst for the degradation of organic pollutants in aqueous solutions [11–15]. However, to the best of the authors' knowledge,

\* Corresponding author.

E-mail address: [victor.delapenya@imdea.org](mailto:victor.delapenya@imdea.org) (V.A. de la Peña O'Shea).

this material has been scarcely used for photocatalytic hydrogen generation [16].

The control of physicochemical and optoelectronic properties is a key factor in the improvement of the performance of this material in photocatalytic reactions, as well as in other applications. These properties are highly influenced by the shape and size of nanoscale semiconductors. Therefore, the synthesis method plays an important role in the control of these characteristics that has been extensively studied by several authors [17–21]. Although the most used procedure to prepare this semiconductor is the solid state method at high temperature, hydrothermal synthesis presents a series of advantages such as improved textural and structural properties and control of the material morphology. Thus, several ZTO nanostructures such as nanoparticles, nanoplates, nanorods, nanobelts and nanowires have been prepared successfully by hydrothermal approaches [17–21].

On the other hand, the use of noble metal nanoparticles as co-catalyst leads to an improvement in the photocatalytic behaviour of these materials [1–3,22,23]. This enhancement may be due to one or more of the following mechanisms: (i) improvement of the charge separation in the semiconductor, (ii) favoured transfer of photogenerated electrons across the metal/semiconductor interface, (iii) promotion of redox pathways with low overpotentials, (iv) co-catalysis of  $H_2$  evolution.

This study reports the photocatalytic  $H_2$  production from methanol aqueous solutions over  $Zn_2SnO_4$  nanostructures prepared by hydrothermal co-precipitation method and loaded with noble metals as co-catalysts. The materials were fully characterised by chemical analysis,  $N_2$  adsorption-desorption isotherms, XRD, Raman, TEM, UV-vis and photoluminescence measurements. *In-situ* photodeposited platinum and gold nanoparticles are used as co-catalyst in order to enhance  $H_2$  production and study their respective effect on the photocatalytic system performance.

## 2. Materials and methods

### 2.1. Synthesis of the photocatalyst

$Zn_2SnO_4$  was prepared by the co-precipitation method using zinc acetate dihydrate ( $Zn(CH_3CO_2)_2 \cdot 2H_2O$ ) and tin tetrachloride pentahydrate ( $SnCl_4 \cdot 5H_2O$ ) as metal precursors. An aqueous solution of both salts with 2:1 Zn:Sn molar ratio was prepared and vigorously stirred at room temperature for 30 min. Subsequently, a 3.5 M solution of  $Na_2CO_3$ , as precipitating agent (PA), was added dropwise to the metal precursors solution for a Zn:Sn:PA molar ratio of 2:1:4. The final solution was vigorously stirred for 15 min, subsequently transferred to a Teflon-lined stainless steel autoclave and heated in an oven at 200 °C for 24 h. The obtained precipitate was filtered, repeatedly washed with deionized water in order to eliminate the remaining by-product salts, dried at 100 °C overnight and finally calcined at 400 °C for 3 h in static air. The product so obtained was named ZTO.

### 2.2. Catalyst characterisation

The metal content was measured by ICP-OES analyses with a Perkin Elmer Optima 3300 DV instrument after digesting the solid in a mixture of HF and  $HNO_3$ . Specific surface areas of the samples were calculated from  $N_2$  adsorption-desorption isotherms that were measured at 77 K on a QUADRASORB instrument after degassing at 250 °C. The samples were characterised by X-ray powder diffraction (XRD) with a Philips PW 3040/00 X'Pert MPD/MRD diffractometer using  $Cu K\alpha$  radiation ( $\lambda = 1.54178 \text{ \AA}$ ) at a scanning rate of  $0.2 s^{-1}$ . The mean crystallite size was determined by the Williamson-Hall equation. Raman spectra were recorded

at room temperature with a JASCO NRS-5000/7000 series Raman spectrometer using an excitation wavelength of 532 nm. A Philips Technai 20 Transmission Electron Microscope, operating with a tungsten filament working at 200 kV, was used to obtain TEM images. Optical measurements were performed using a DRS UV/Vis/NIR Perkin Elmer Lambda 1050 Spectrometer, while photoluminescence experiments were carried out on a Fluorescence Spectrometer Perkin Elmer LS 55, with an excitation wavelength of 280 nm and using a cut-off filter at 350 nm.

### 2.3. Photocatalytic reaction equipment

Hydrogen production experiments were conducted in a slurry photoreactor, which consisted of a three-mouth cylindrical flask made of glass with an effective volume of 1 L. For the experiments, 0.2 g of photocatalyst was added to a 10 vol.% methanol aqueous solution. After that, the reactor was tightly closed and maintained at a temperature of 20 °C by a cooling system. The reaction temperature was measured with a thermocouple situated on the photoreactor wall. Argon was then flown through the suspension at 30 mL/min and atmospheric pressure. The suspension was magnetically stirred in the dark until air was removed (verified by GC) and then irradiated by a 150 W medium-pressure Hg UV lamp for 7 h.  $H_2$  evolution was monitored every ca. 4.5 min by means of a Varian micro-GC equipped with two channels with a molecular sieve and a PPQ column, respectively.

For the reactions with Pt or Au as co-catalysts, the metals were photodeposited *in-situ* on ZTO in the photoreactor by dissolving the appropriate amount of  $H_2PtCl_6 \cdot xH_2O$  or  $HAuCl_4 \cdot xH_2O$  in the reaction medium before adding the photocatalyst. Nominal Pt loadings were 0.5, 1, 2 or 4 wt.% (denoted as Pt/ZTO-I, Pt/ZTO-II, Pt/ZTO-III and Pt/ZTO-IV, respectively) while that of Au was 0.5 wt.% (Au/ZTO).

## 3. Results and discussion

### 3.1. Physico-chemical characterisation of the catalysts

$Zn_2SnO_4$  (ZTO), Pt/ZTO and Au/ZTO catalysts were characterised by several physico-chemical techniques and tested for photocatalytic hydrogen production from aqueous methanol solutions.

Fig. 1 shows the XRD patterns of the synthesised materials. In the case of bare ZTO, the observed diffraction peaks can be indexed to a  $Zn_2SnO_4$  phase with inverse cubic spinel structure (JCPDS PDF file 24–1470) corresponding to a space group  $Fd\bar{3}m$ , with lattice parameter  $a = 8.679 \text{ \AA}$  and cell volume  $V_{cell} = 653.7 \text{ \AA}^3$ . In this structure, half of the  $Zn^{2+}$  cations are in tetrahedral sites, while the other half and  $Sn^{4+}$  cations are in octahedral ones. This inverse spinel structure is typically obtained by the hydrothermal method [24–27]. However, previous studies have shown that, depending on the synthesis conditions, other crystal phases or a distortion of this cubic structure leading to a hexagonal one ( $R\bar{3}m$ ) can be observed [24]. None of these polymorphs was detected under the current synthesis conditions, which were carefully chosen according to previously reported results.

Thus, the nature and the concentration of the precipitating agent have a great influence on the physicochemical properties of ZTO. Previous studies [28,29] showed that the use of a mild base like  $Na_2CO_3$  leads to a higher control of the textural, structural and morphological properties of ZTO materials. Strong bases (e.g. NaOH) promote the formation of intermediate phases such as  $ZnSn(OH)_6$ , highly stable and difficult to transform into  $Zn_2SnO_4$  during the hydrothermal treatment [14,28], while moderately alkaline reagents such as  $Na_2CO_3$ , hydrazines, amines or low concentrations of NaOH facilitate the formation of Sn and Zn hydroxides that are more easily converted into ZTO [24,25,28].

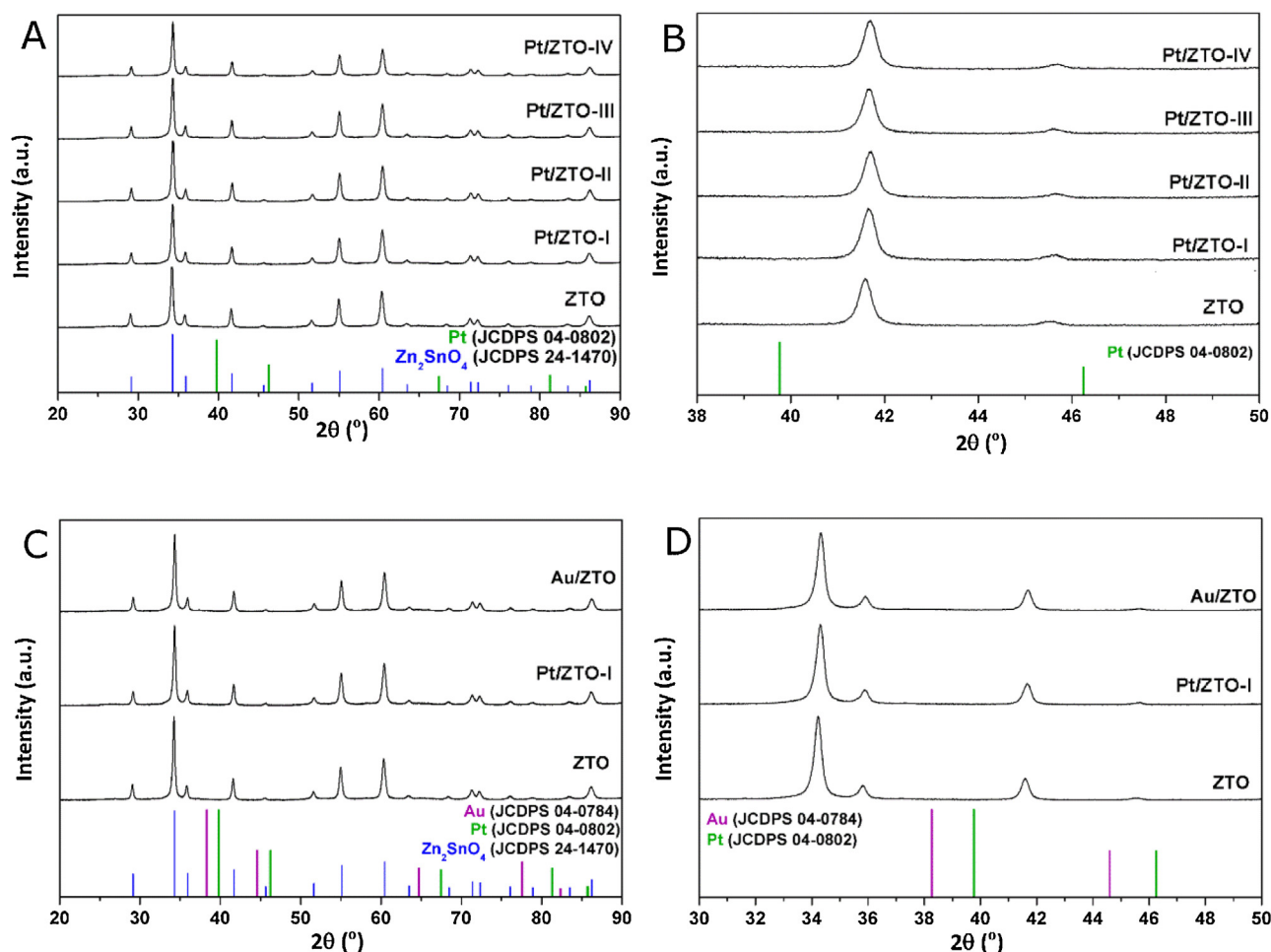


**Fig. 1.** XRD patterns of the obtained photocatalysts: (a) ZTO and Pt/ZTO catalysts; (b) magnification of (a) in the 38–50°  $2\theta$  region; (c) comparison of bare, Pt- and Au-loaded ZTO; (d) magnification of (c) in the 30–50°  $2\theta$  region.

Regarding the base concentration, this factor affects the solubility of the precursor during the dissolution-recrystallization processes in the hydrothermal synthesis. In fact, Annamalai et al. [28,29] obtained high purity and well crystallized materials using Zn:Sn:PA ratios of 2:1:4. Lower and higher amount of precipitating agent lead to less crystalline and more agglomerated ZTO, respectively. Finally, the temperature for hydrothermal treatment was chosen at 200 °C so that particulate nucleation is favoured rather than growth, leading to smaller particle sizes [14,15].

In the present work, as a result of all synthesis settings, single-phase, well-crystallized ZTO with relatively low mean crystal size was obtained. In the case of the XRD of metal-containing samples (Fig. 1b and d), with both Pt and Au co-catalysts the diffraction peaks of the metal or any Pt or Au oxide phases are absent, which may be indicative of an efficient dispersion of co-catalyst nanoparticles. In addition, no changes in the ZTO structure are observed after metal photodeposition and subsequent photocatalytic  $\text{H}_2$  production reaction.

The structural characterisation was completed by Raman spectroscopy (Fig. 2). The ZTO bare sample shows the two characteristic peaks of this inverse spinel cubic phase. The strongest Raman active mode at  $675\text{ cm}^{-1}$  corresponds to the stretching vibration of M–O short bonds in the octahedral metal site and the peak at  $537\text{ cm}^{-1}$  is due to the oxygen vibration in the tetrahedral one [13,14]. These bands are also detected in the metal-decorated catalysts. However, the quality of the signal is lower, probably due to an increase in the surface covering by the metal NPs that diminishes the Raman

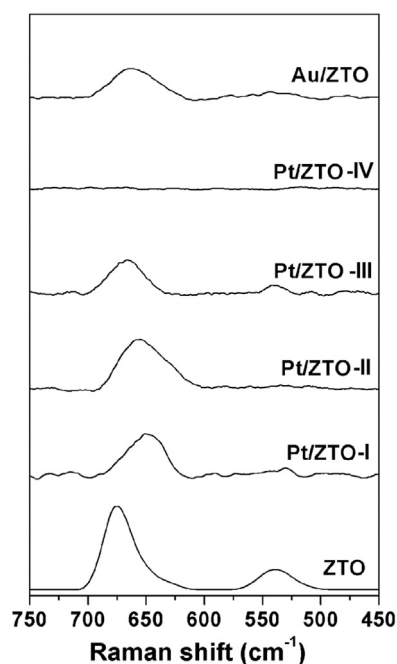


**Fig. 2.** Raman spectra of ZTO and M/ZTO (M = Pt or Au) photocatalysts.

signal. This behaviour is more pronounced when the metal loading increases, and in the case of the highest loading (Pt/ZTO-IV) the Raman peaks even disappear.

Fig. 3A and B depict the TEM images of ZTO catalyst, which is formed by aggregates of pseudo-spherical and, in a lower proportion, cuboctahedral nanoparticles (with hexagonal shape in projection), with sizes in the range of 20–50 nm. In an interesting work, Jiang et al. [24] showed that the basicity, ionic character and concentration of the alkaline mineralizer plays a determining role in the morphology (cubic, cuboctahedral, truncated octahedral, or irregular shapes) and size distribution (20–1500 nm) of hydrothermally synthesised ZTO particles. In this work, using sodium carbonate as a mild basic precipitating agent, TEM images of the obtained ZTO reveal lattice fringes corresponding to the (111) crystal planes with a  $d$  spacing of 0.495 Å. This may corroborate the formation of cuboctahedral nanoparticles that possess six (100) and eight (111) facets [24]. Furthermore, these NPs have attached other small irregular nanoparticles with sizes below 5 nm. This bimodal distribution is congruent with dissolution-recrystallization mechanisms and growth through an Ostwald ripening process, which occurs during the hydroxide precursor transformation in the hydrothermal treatment [14,16]. The TEM images of metal-decorated samples exhibit small dark spots assigned to metal nanoparticles (using EDX) homogeneously distributed over the semiconductor surface. In the case of Pt, the increase of the metal loading leads to a higher covering of the ZTO surface and increase in the particle size (Fig. 4). Between the minimum and maximum loadings (Table 1), the maximum of the crystallite size distribution changes from 2 to 5 nm, although a monotonic particle size increase with Pt loading is not observed. On the other hand, the gold-containing catalyst (Fig. 5) shows a bimodal distribution of metal sizes centred at 5 and 10 nm, larger sizes than in the case of Pt, which indicates a poorer dispersion of the metal.

Textural properties of ZTO and supported samples were evaluated by  $N_2$  adsorption-desorption isotherms (Table 1). All materials present “type II” isotherms (not shown), which indicates that they are non-porous and the specific surface area ( $S_{BET}$  ZTO = 38 m<sup>2</sup>/g) is due to the external surface of the particles. Furthermore, the observed hysteresis loop at high  $P/P_0$  reveals the presence of macropores corresponding to interparticle voids. This behaviour is analogous to that obtained in previous works with similar preparation procedures [15,28,29]. The pore sizes correspond to a unimodal distribution with values in the 20–30 nm range.

The band structure and opto-electronic properties of ZTO materials have been extensively studied by different electrochemical, optical and photoelectrochemical techniques [12,30,31]. The published band gaps vary from 3.35 to 4.1 eV. These dissimilarities can be explained by differences in the measurement method and also by the intrinsic physicochemical properties of the ZTO materials (chemical composition, structure, morphology and quantum size effects). Regarding the semiconductor type transition, most of the published papers assume that this material possesses a direct transition [14,28], while other studies, including experimental and theoretical calculations, suggest that it is an indirect semiconductor [26,32]. In any case, the most observed values for the band gap are estimated between 3.6 and 3.7 eV [14,26,30] for bulk materials, while in thin films the published values range from 3.35 to 3.85 eV [33,34] due to the Burstein-Moss shift.

The UV–vis diffuse reflectance spectra of the materials prepared in this work are shown in Fig. 6. The ZTO catalyst presents a strong absorption in the UV region with a band edge at around 370 nm. The band gap was calculated using a Tauc plot, assuming both a direct and an indirect transition, and the obtained values are 3.79 and 3.44 eV, respectively, which are in good agreement with those reported in the previous works mentioned above. After Pt addition

on the semiconductor surface, the absorbance increases in the visible region, showing a rather continuous absorption that grows for higher metal loading. On the other hand, the Au/ZTO catalyst exhibits a new absorption band in the visible region centred at 560 nm. This band is attributed to the Surface Plasmon Resonance (SPR) effect of Au<sup>0</sup> NPs. The presence in all cases of metal NPs indicate the reduction of the precursors of these metals during the photodeposition method due to the transfer of photoexcited electrons from the ZTO conduction band (CB) [35]. The metal deposition on these materials does not change the band-gap of ZTO itself.

Photoluminescence (PL) spectra of all samples are shown in Fig. 7. All materials show similar emission bands due to the transition between the energy levels of the ZTO semiconductor but with different intensities. The emission spectrum of the bare semiconductor shows a broad band that covers the region from 350 to 700 nm. Taking into account that the band-gap of bulk ZTO is between 3.6 and 3.7 eV and the used cut-off filter is at 350 nm, only the tail of the band-to-band transition emission peak is observed in the spectrum. Previous studies have assigned these bands to oxygen vacancies emission centres or residual strain due to the crystal defects and interstitial Zn appearing during the growth process [13,14,30]. In this sense, in the studies performed by Wang et al. [13,36] using the annealing method to produce oxygen vacancies in ZTO, the increase in the vacancies led to an enhancement in the intensity of the emission peaks. Moreover, those vacancies induced the formation of intermediate energy levels giving rise to a red shift in the PL bands. Photoluminescence (PL) spectra of metal M/ZTO (where M is Pt or Au) are also shown in Fig. 7. The PL intensity decreases with metal deposition, suggesting a lowering in the electron-hole recombination rate which can be ascribed to metal nanoparticles acting as electron traps. In the case of Pt-containing catalysts, the decrease in the PL intensity is more marked for higher loadings. Changing the metal to Au leads to a lower decrease in the emission intensity in comparison with Pt, even if the real Pt loading in the Pt/ZTO-I sample is around 1.5 times less than in the corresponding Au-containing sample (Table 1). Therefore, this indicates that Pt is more effective as electron scavenger.

### 3.2. Catalytic performance

Fig. 8 shows the accumulated  $H_2$  productions and the steady-state production rates over ZTO and Pt/ZTO catalysts. Under dark conditions, or under UV irradiation without photocatalyst, no  $H_2$  evolution was detected. ZTO bare sample shows the lowest  $H_2$  production. This fact could be attributed to a high recombination rate of photogenerated electrons and holes (see PL section). Nevertheless, the activity of bare ZTO is comparatively higher than those reported in the literature in the methanol/water system with ZnO [37–39], and comparable to that of NaTaO<sub>3</sub> [40]. The production rate increases during the first 2 h and then remains constant. This behaviour was previously described by Fu et al. [14] and was assigned to the increase of ZTO dispersion by the separation of small ZTO nanoparticles due to the stirring of the solution. However, the time needed in the present experiments to reach the maximum rate is considerably shorter than the one reported there, and similar to that observed with a pre-stirred sample [14], suggesting that a good dispersion is already attained in the present catalyst without any pre-treatment.

With Pt-containing catalysts, the zero-production period observed after irradiation starts corresponds to the reduction reaction of Pt(IV) species to form the Pt nanoparticles on the ZTO surface, and is expectedly longer for higher Pt loadings. Over these catalysts,  $H_2$  production is dramatically increased in all cases, with actual improvements depending on the co-catalyst relative amount. Thus, Pt/ZTO-I increases the  $H_2$  production by a factor of 15 with respect to ZTO, up to 398  $\mu\text{mol g}_{\text{cat}}^{-1}$ , or 80  $\mu\text{mol } H_2$



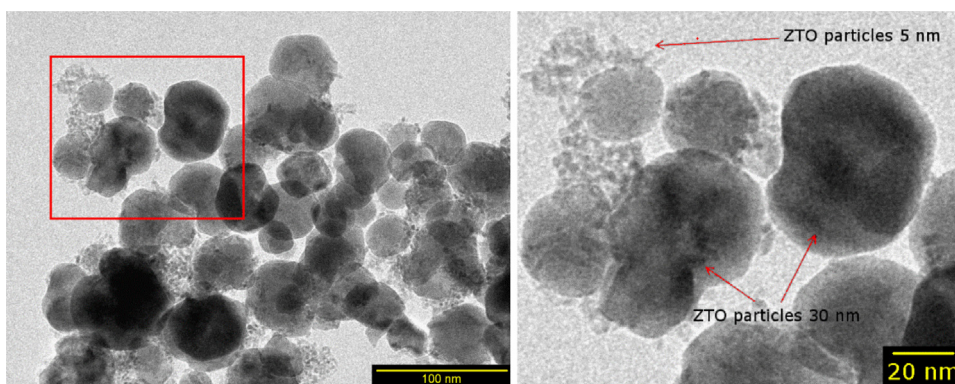


Fig. 3. TEM image of ZTO (left). Magnification of the marked area (right).

Table 1

Chemical, structural and morphological characteristics of the prepared catalysts.

Catalyst	Metal loading (wt%)	$S_{\text{BET}}$ ( $\text{m}^2\text{g}^{-1}$ )	$D_{\text{pore}}$ (nm)	$d$ (nm) <sup>a</sup> ZTO	$a = b = c$ (Å) ZTO	$V_{\text{cell}}$ ( $\text{\AA}^3$ ) ZTO	$d$ (nm) <sup>b</sup> metal
ZTO	–	38	20	39	8.679	653.733	–
Pt/ZTO-I	0.29	44	28	48	8.676	653.181	2.3
Pt/ZTO-II	0.65	50	19	44	8.672	652.080	2.8–3.4
Pt/ZTO-III	1.36	42	18	29	8.669	651.530	2.5–3.0
Pt/ZTO-IV	2.78	47	27	57	8.667	650.981	5.2
Au/ZTO	0.45	40	29	50	8.661	649.687	5.8 – 9.6

<sup>a</sup> Determined from XRD patterns with Williamson–Hall plots.

<sup>b</sup> Center of the particle size distribution measured from TEM images. The cases with two values correspond to bimodal distributions.

in absolute terms. Further Pt loading, however, does not result in a correspondingly higher photocatalytic activity. Pt/ZTO-II sample leads to a slightly lower hydrogen production than Pt/ZTO-I, while higher loadings, as represented by Pt/ZTO-III and Pt/ZTO-IV catalysts, give rise to a gradual decrease in activity with respect to lower Pt contents (Table 1). The steady-state rate values shown in Fig. 8(D) correspond to apparent quantum yields between 0.04% (ZTO) and 0.53% (Pt/ZTO-I) in the present irradiation conditions. It is important to recall as well that no sign of catalyst deactivation is observed with any of the catalysts, which indicates the stability of  $\text{Zn}_2\text{SnO}_4$  under reaction conditions. In line with this, to further corroborate reusability, Pt/ZTO-I recovered from the photocatalytic reaction was reused and subjected to UV-dark cycles. As observed in Fig. 9, the catalyst retains activity after several uses.

Therefore, a benefit of the presence of Pt co-catalyst in the activity of the photocatalytic system is clear from the above described results, with the best performance with loading of ca. 0.3 wt%, as determined experimentally in the Pt/ZTO-I sample (Table 1). If the produced amounts of  $\text{H}_2$  are referred to the metal content, a better utilisation of the deposited Pt is further evident at lower loadings. Here, a divergence with previous results appears with respect to the effect of Pt on the activity of ZTO photocatalysts. Indeed, Fu et al. [14] observed a decrease in the  $\text{H}_2$  evolution rate upon deposition of 1 wt.% Pt on ZTO with respect to the bare semiconductor, which they ascribed to unfavourable work functions and electrical contact between  $\text{Zn}_2\text{SnO}_4$  and Pt. The results exposed here go in a rather different direction therefore.

As mentioned in the introduction, the effect of co-catalysts in photocatalytic reactions may occur following different physico-chemical pathways. In the case of platinum, the observed enhancements are generally ascribed to the performance of Pt NP's as electron traps, reducing the electron-hole recombination rate [1,41]. In the same line, transient absorption spectroscopy (TAS) experiments have shown the electro-discharge capability of Pt nanoparticles [42]. The photoluminescence spectra reported in this work corroborate this assumption, in contrast to the sugges-

tion by Fu et al. that the work function of ZTO is not appropriate for such transfer [14]. Therefore, the positive effect of Pt deposition observed here can be at least partially explained in such terms. In addition to this, Pt is well known as a hydrogen evolution catalyst, and recently a dominant effect of this characteristic has been proposed to account for its role in photocatalytic hydrogen production [23]. Nevertheless, some authors have suggested that the positive role of platinum is highly dependent on the metal cluster size, so that when it becomes sufficiently large this beneficial aspect is lost, whereby the Pt NPs can act as recombination centres [43,44]. Regarding co-catalyst loading, higher amounts should lead to higher reaction rates provided that the metal particles are well dispersed. However, undue amounts or poor metal distribution may also increase recombination and, at the same time, provoke a shading effect hindering light absorption by the semiconductor [41], which can be indeed envisaged in the UV-vis spectra. A compromise between these structural/morphological aspects may lead in this case to the best performance in the Pt/ZTO-I catalyst.

Depending on the metal, different co-catalyst behaviours are observed; thus, Pt and Pd provide an ohmic contact, while other metals such as Ag and Au exhibit capacitive properties. In the general case of a metal/semiconductor system, it is known that UV light leads to a decrease in the metal Fermi level (more negative potential), which approaches the conduction band due to the electron storage. This change is due to an electronic transfer from the semiconductor to the metallic NPs, leading to an excess of negative charge in the metal and a positive charge in the semiconductor. As a result, a Schottky barrier is formed between the semiconductor conduction band and the metal Fermi level. Some studies have shown that the shift in the Fermi level could be as high as 0.1 V per stored electron in a nanoparticle [45–47]. This shift allows the photogenerated electrons in the semiconductor to be trapped on the metal nanoparticles, improving the charge separation. Smaller particle size was found to induce a maximum shift in the Fermi level of the metal/semiconductor system. Radiative recombination occurs in the range of picoseconds for bare semiconductors, while in the

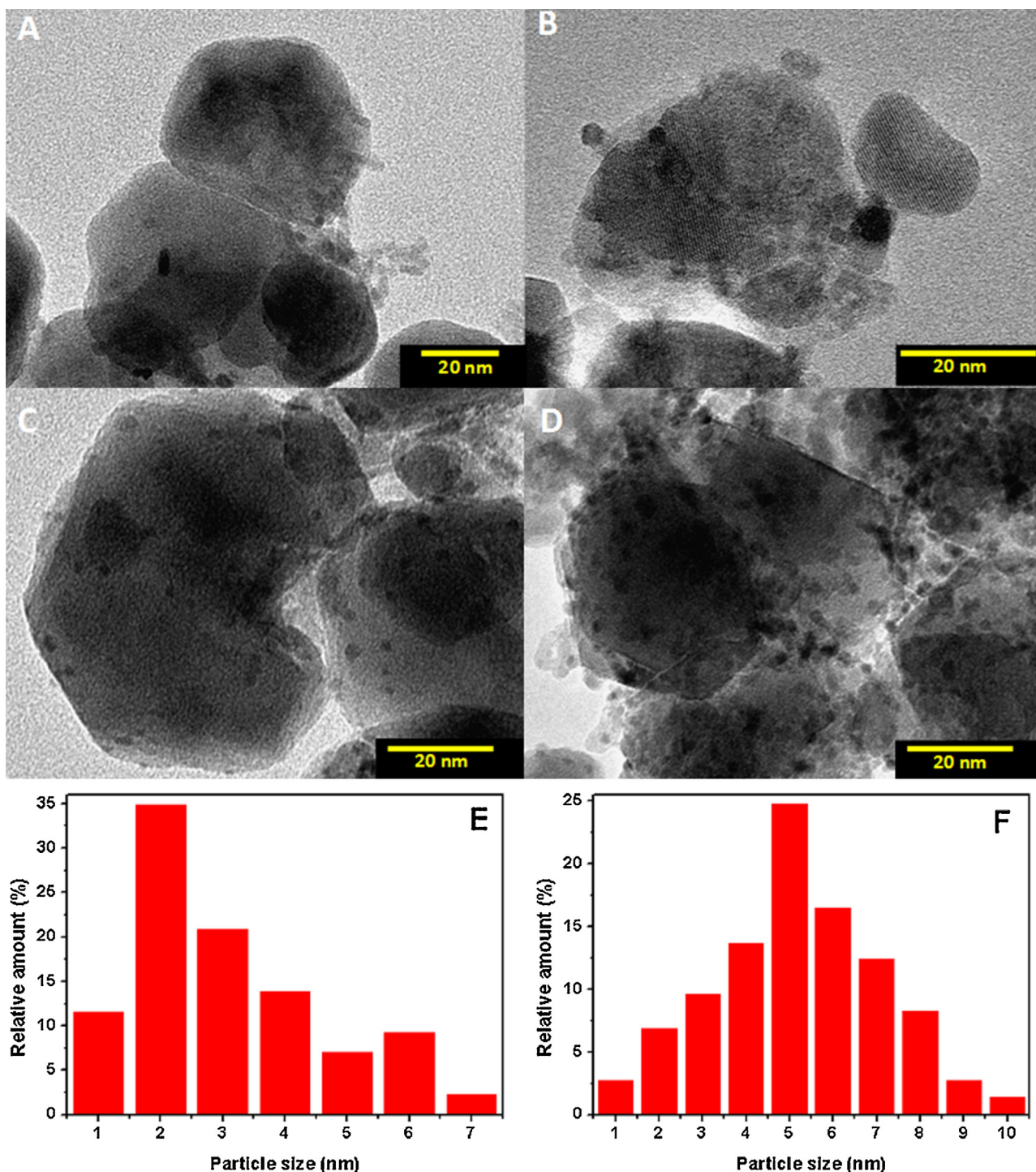


**Fig. 4.** (A–D) TEM images of Pt/ZTO-I, Pt/ZTO-II, Pt/ZTO-III and Pt/ZTO-IV, respectively. (E, F) Pt particle size distribution (obtained from several TEM images) in Pt/ZTO-I and Pt/ZTO-IV, respectively.

case of trapped photoelectrons, it happens at the nanosecond to microsecond scale, depending on the size of metal and support. A decrease in the semiconductor particle size may increase the recombination rate of trapped electrons. Regarding metal particles, a decrease in the size leads to a higher modification in the Fermi level towards more negative potentials, provoking an increase in the photogenerated electrons lifetime.

As in the case of platinum, Au nanoparticles can act as electron scavengers [45], but the latter exhibits capacitive properties [48]. Electron accumulation of Au/TiO<sub>2</sub> catalyst is produced by the

above-mentioned shift from the Au Fermi level (+0.45 vs NHE) to more negative potentials; this change is also observed in Au/ZnO catalysts [49,50]. In order to compare the effect of Au nanoparticles as co-catalyst on the activity of Zn<sub>2</sub>SnO<sub>4</sub> with that of Pt, a Au/Zn<sub>2</sub>SnO<sub>4</sub> photocatalyst with nominal 0.5% Au was tested for the methanol reforming reaction. Fig. 8 shows the H<sub>2</sub> production obtained with Pt/ZTO-I and Au/ZTO. The results show that Au is considerably less active as co-catalyst than Pt, giving rise to a produced amount of hydrogen nearly one order of magnitude lower. Nevertheless, the activity of Au/ZTO is still higher than that of ZTO itself.



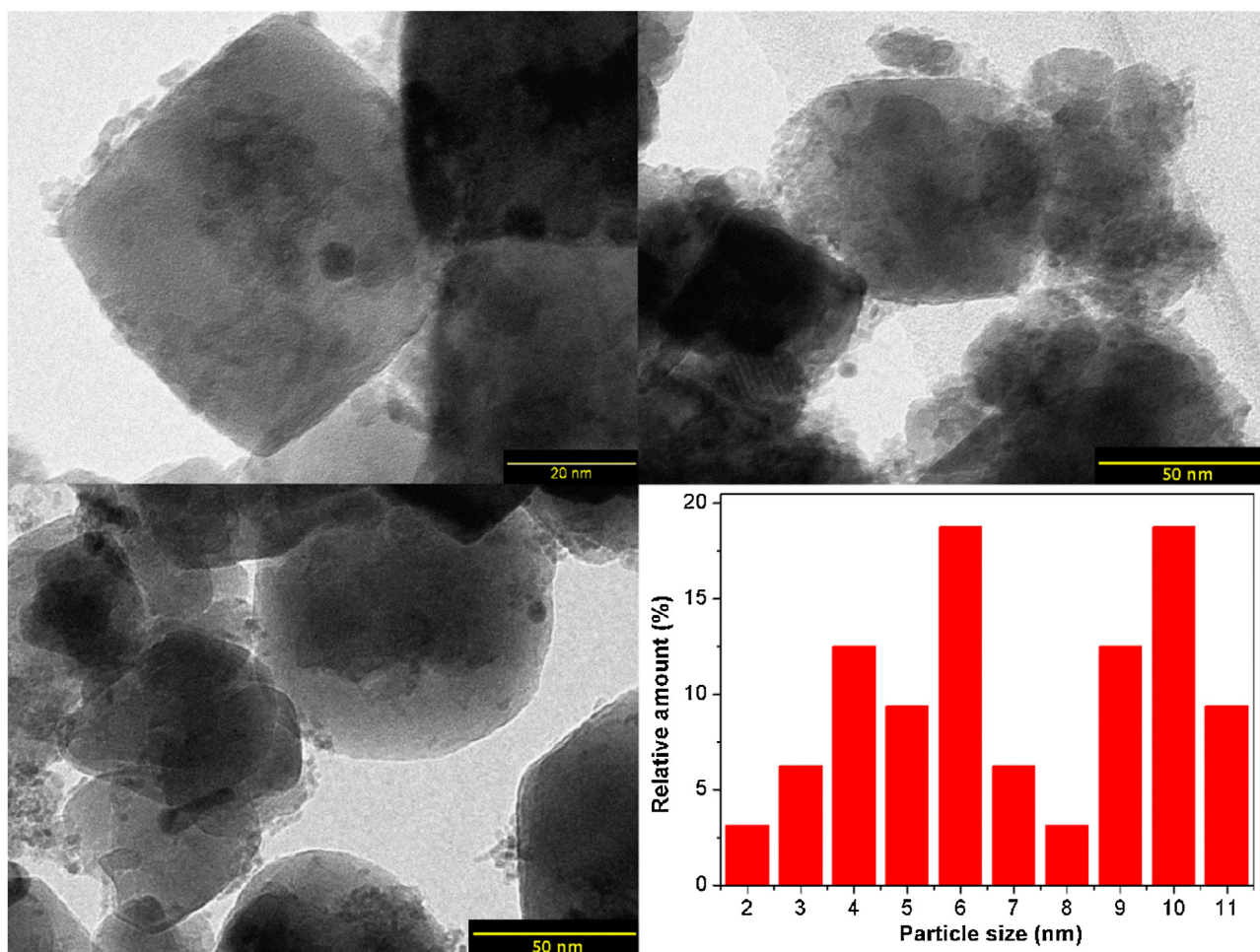


Fig. 5. TEM images and Au particle size distribution of Au/ZTO.

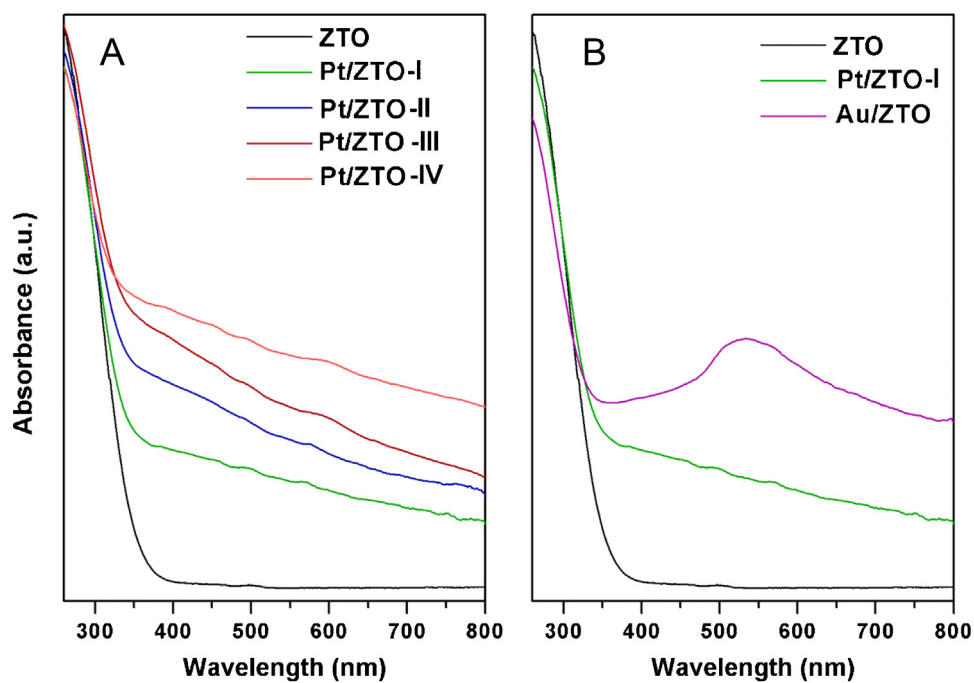


Fig. 6. (A) Uv-vis spectra of ZTO and Pt/ZTO samples. (B) Compared spectra of ZTO, Pt/ZTO-I and Au/ZTO.

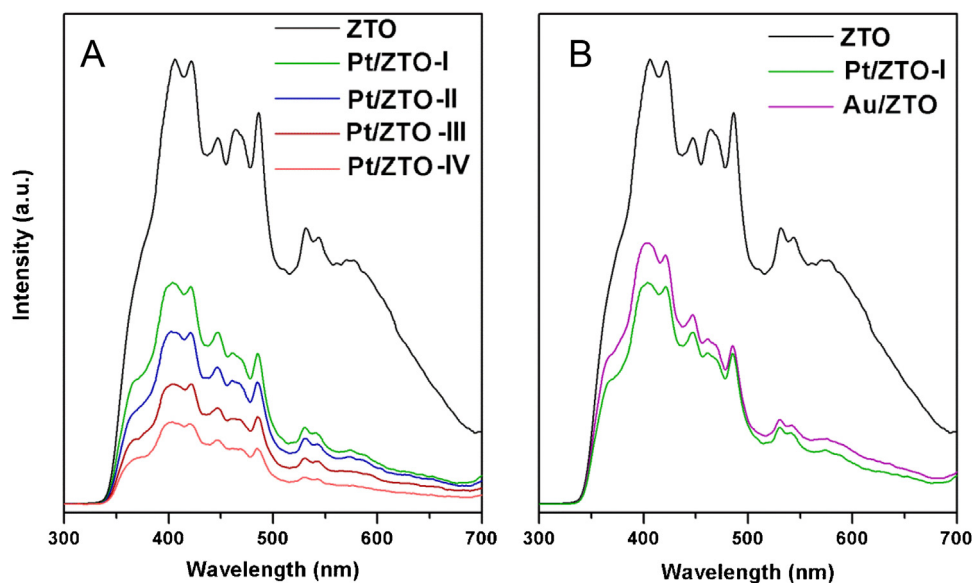


Fig. 7. (A) Photoluminescence spectra of ZTO and Pt/ZTO samples. (B) Compared spectra of ZTO, Pt/ZTO-I and Au/ZTO.

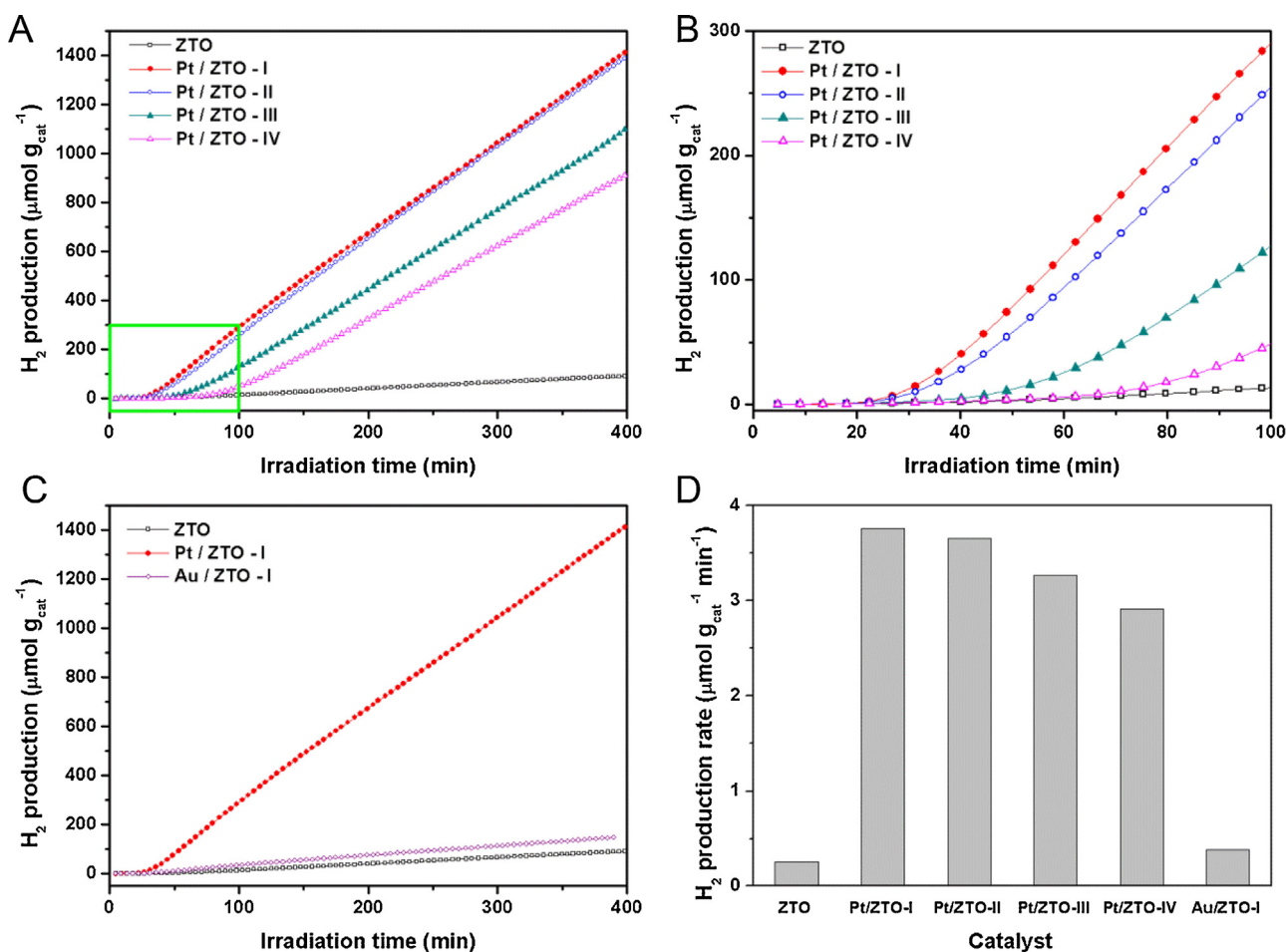


Fig. 8. (A) Cumulative  $H_2$  production over ZTO and Pt/ZTO catalysts; (B) Magnification of the area marked in (A); (C) Cumulative  $H_2$  production over ZTO, Pt/ZTO-I and Au/ZTO catalysts; (D) steady-state  $H_2$  production rates with all catalysts.

Assuming a lower electron-hole recombination as the main effect governing the activity of metal/ZTO systems (vide supra), these results are in agreement with those observed in photoluminescence spectra (Fig. 7). In addition,  $\text{TiO}_2$ -supported Au nanoparticles

have been observed to be less active than Pt ones for the recombination of hydrogen atoms [23], which may also contribute to their lower activity as hydrogen evolution co-catalyst observed in the present system.



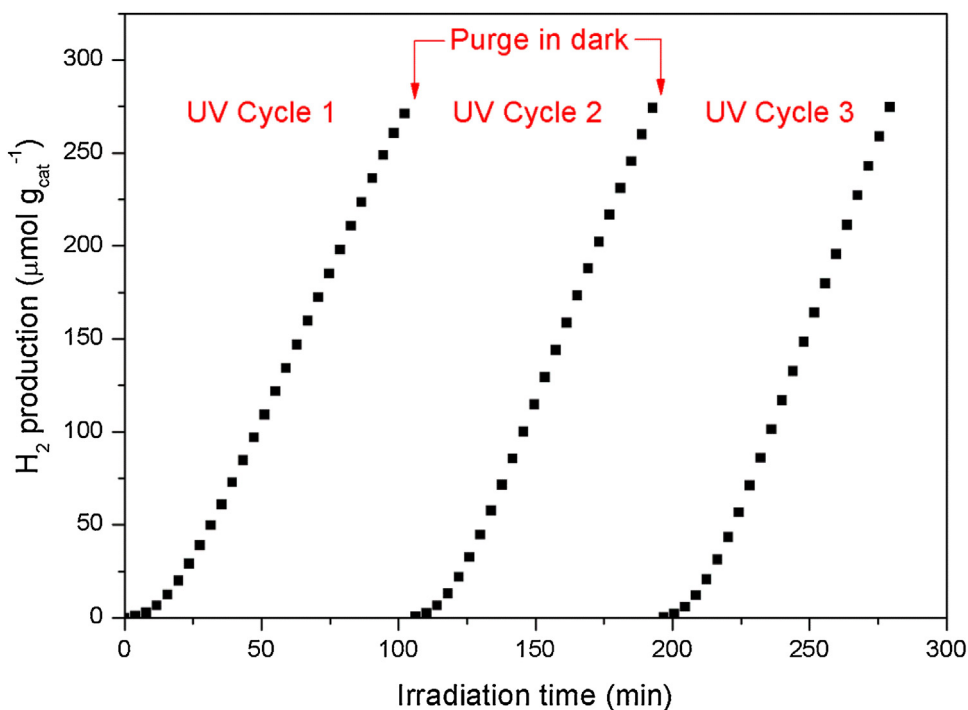


Fig. 9. Cumulative H<sub>2</sub> production over re-used Pt/ZTO-I during UV-dark cycles.

#### 4. Conclusions

Although bare Zn<sub>2</sub>SnO<sub>4</sub> nanostructures have shown little activity for photocatalytic hydrogen evolution from aqueous methanol solutions, the reaction proceeds without apparent catalyst deactivation during the tested reaction time. Deposition of Pt on the ZTO surface, on the other hand, dramatically increases the activity of this mixed oxide, with the best performance obtained with an experimental 0.3 wt.% of Pt, while the absence of deactivation is maintained and the catalyst shows good reusability and cyclability. Higher loadings lead to lower H<sub>2</sub> production, which is ascribed to poorer metal distribution and a shading effect of the excess metal. On the other hand, gold nanoparticles give rise to considerably lower activity than platinum ones, with a H<sub>2</sub> production ca. 10 times lower with the former than with the latter at the same nominal wt.% coverage. A more efficient charge separation effect, based on photoluminescence measurements, and the lower activity of Au for H–H bond formation compared to Pt, are invoked to account for the observed results.

#### Acknowledgements

Financial support from the Spanish Ministry of Economy and Competitiveness (project CTQ2014-51487-ERC) is gratefully acknowledged. V.A.P.O., L.C. and P.J. thank funding support from the grants “Ramón y Cajal”, FPI and “Juan de la Cierva”, respectively. F.F. thanks financial support from the *Amarout-II* PEOPLE-COFUND Marie Skłodowska-Curie Action.

#### References

- [1] M.D. Hernández-Alonso, F. Fresno, S. Suárez, J.M. Coronado, *Energy Environ. Sci.* 2 (2009) 1231–1257.
- [2] D.P. Serrano, J.M. Coronado, V.A. de la Peña O’Shea, P. Pizarro, J.A. Botas, *J. Mater. Chem. A* 1 (2013) 12016–12027.
- [3] A. Kudo, Y. Miseki, *Chem. Soc. Rev.* 38 (2009) 253–278.
- [4] D.P. Serrano, G. Calleja, P. Pizarro, P. Gálvez, *Int. J. Hydrogen Energy* 39 (2014) 4812–4819.
- [5] Y. Zheng, L. Lin, B. Wang, X. Wang, *Angew. Chem. Int. Ed.* 54 (2015) 12868–12884.
- [6] A. Wolcott, W.A. Smith, T.R. Kuykendall, Y. Zhao, J.Z. Zhang, *Adv. Funct. Mater.* 19 (2009) 1849–1856.
- [7] H.M. Chen, C.K. Chen, Y.C. Chang, C.W. Tsai, R.S. Liu, S.F. Hu, W.S. Chang, K.H. Chen, *Angew. Chem. Int. Ed.* 49 (2010) 5966–5969.
- [8] X. Wang, G. Liu, G.Q. Lu, H.-M. Cheng, *Int. J. Hydrogen Energy* 35 (2010) 8199–8205.
- [9] C.H. Park, S.B. Zhang, S.H. Wei, *Phys. Rev. B* 66 (2002) 073202.
- [10] K. Maeda, K. Teramura, N. Saito, Y. Inoue, K. Domen, *J. Catal.* 243 (2006) 303–308.
- [11] Y. Yamada, Y. Seno, Y. Masuoka, K. Yamashita, *Sens. Actuators B Chem.* 49 (1998) 248–252.
- [12] B. Tan, E. Toman, Y. Li, Y. Wu, *J. Am. Chem. Soc.* 129 (2007) 4162–4163.
- [13] J.X. Wang, S.S. Xie, H.J. Yuan, X.Q. Yan, D.F. Liu, Y. Gao, Z.P. Zhou, L. Song, L.F. Liu, X.W. Zhao, X.Y. Dou, W.Y. Zhou, G. Wang, *Solid State Commun.* 131 (2004) 435–440.
- [14] J. Zeng, M. Xin, K.W. Li, H. Wang, H. Yan, W. Zhang, *J. Phys. Chem. C* 112 (2008) 4159–4167.
- [15] W. Cun, W. Xinming, Z. Jincai, M. Bixian, S. Guoying, P. Ping’an, F. Jiamo, *J. Mater. Sci.* 37 (2002) 2989–2996.
- [16] X. Fu, X. Wang, J. Long, Z. Ding, T. Yan, G. Zhang, Z. Zhang, H. Lin, X. Fu, *J. Solid State Chem.* 182 (2009) 517–524.
- [17] Y. Zhang, J. Wang, H. Zhu, H. Li, L. Jiang, C. Shu, W. Hu, C. Wang, *J. Mater. Chem.* 20 (2010) 9858–9860.
- [18] Z.J. Wang, J. Liu, F.J. Wang, S.Y. Chen, H. Luo, X.B. Yu, *J. Phys. Chem. C* 114 (2010) 13577–13582.
- [19] J. Chen, L. Lu, W. Wang, *J. Phys. Chem. C* 116 (2012) 10841–10847.
- [20] J.X. Wang, X.W. Sun, S.S. Xie, W.Y. Zhou, Y. Yang, *Cryst. Growth Des.* 8 (2008) 707–710.
- [21] G.X. Ma, R.J. Zou, L. Jiang, Z.Y. Zhang, Y.F. Xue, L. Yu, G.S. Song, W.Y. Li, J.Q. Hu, *CrystEngComm* 14 (2012) 2172–2179.
- [22] P.V. Kamat, *J. Phys. Chem. B* 106 (2002) 7729–7744.
- [23] J.B. Joo, R. Dillon, I. Lee, Y. Yin, C.J. Bardeen, F. Zaera, *Proc. Natl. Acad. Sci. U. S. A.* 111 (2014) 7942–7947.
- [24] T.Q. Jiang, X.X. Chen, R. Sun, Z. Xiong, L.S. Zheng, *Mater. Chem. Phys.* 129 (2011) 53–61.
- [25] S.J. Fang, A. Huang, P. Zhu, N. Xu, J. Xie, J. Chi, S. Feng, R. Xu, M. Wu, *Mater. Res. Bull.* 36 (2001) 1391–1397.
- [26] M.A. Alpuche-Aviles, Y. Wu, *J. Am. Chem. Soc.* 131 (2009) 3216–3224.
- [27] T. Lana-Villarreal, G. Boschloo, A. Hagfeldt, *J. Phys. Chem. C* 111 (2007) 5549–5556.
- [28] A. Annamalai, D. Carvalho, K.C. Wilson, M.-J. Lee, *Mater. Charact.* 61 (2010) 873–881.
- [29] A. Annamalai, D. Carvalho, K.C. Wilson, M.-J. Lee, *Mater. Charact.* 62 (2011) 1007–1015.
- [30] H.F. Lin, S.C. Liao, S.W. Hung, C.T. Hu, *Mater. Chem. Phys.* 117 (2009) 9–13.
- [31] C. Pang, B. Yan, L. Liao, B. Liu, Z. Zheng, T. Wu, H. Sun, T. Yu, *Nanotechnology* 21 (2010) 465706.

- [32] D. Segev, S.H. Wei, *Phys. Rev. B* 71 (2005) 125129–125141.
- [33] E. Çentinörgü, *Opt. Commun.* 280 (2007) 114–119.
- [34] H. Young, Y. Yan, T.J. Coutts, *J. Appl. Phys.* 92 (2002) 310–319.
- [35] L. Collado, P. Jana, B. Sierra, J.M. Coronado, P. Pizarro, D.P. Serrano, V.A. de la Peña O'shea, *Chem. Eng. J.* 224 (2013) 128–135.
- [36] J.X. Wang, S.S. Xie, Y. Gao, X.Q. Yan, D.F. Liu, H.J. Yuan, Z.P. Zhou, L. Song, L.F. Liu, W.Y. Zhou, G. Wang, *J. Cryst. Growth* 267 (2004) 177–183.
- [37] Z. Liu, H. Bai, S. Xu, D.D. Sun, *Int. J. Hydrogen Energy* 36 (2011) 13473–13480.
- [38] A.M. Hussein, R.V. Shende, *Int. J. Hydrogen Energy* 11 (2014) 5557–5568.
- [39] P. Gomathisankar, K. Hachisuka, H. Katsumata, T. Suzuki, K. Funasaka, S. Kaneco, *Int. J. Hydrogen Energy* 38 (2013) 11840–11846.
- [40] P. Jana, C. Mata Montero, P. Pizarro, J.M. Coronado, D.P. Serrano, V.A. de la Peña O'shea, *Int. J. Hydrogen Energy* 39 (2014) 5283–5290.
- [41] V.A. de la Peña O'Shea, J.M. Coronado, F. Fresno, M.D. Hernández-Alonso, R. Portela (Eds.), *Design of Advanced Photocatalytic Materials for Energy and Environmental Applications*, Springer, London, 2013 (ISBN: 978-1-4471-5060-2. Ch. 10).
- [42] C. Harris, P.V. Kamat, *ACS Nano* 4 (2010) 7321–7330.
- [43] H. Gerisher, *Photocatalytic Purification and Treatment of Water and Air*, in: D.F. Ollis, H. Al-Ekabi (Eds.), Elsevier Science Publishers B.V., New York, 1993.
- [44] M. Sadeghi, W. Liu, T.-G. Zhang, P. Stavropoulos, B. Levy, *J. Phys. Chem.* 100 (1996) 19466–19474.
- [45] S. Chen, R.S. Ingram, M.J. Hostetler, J.J. Pietron, R.W. Murray, T.G. Schaaff, J.T. Khoury, M.M. Alvarez, R.L. Whetten, *Science* 280 (1998) 2098–2101.
- [46] A. Takai, P.V. Kamat, *ACS Nano* 5 (2011) 7369–7376.
- [47] A.C. Templeton, W.P. Wuelfing, R.W. Murray, *Acc. Chem. Res.* 33 (2000) 27–36.
- [48] P.V. Kamat, *J. Phys. Chem. Lett.* 3 (2012) 663–672.
- [49] V. Subramanian, E. Wolf, P.V. Kamat, *J. Phys. Chem. B* 107 (2003) 7479–7485.
- [50] A. Wood, M. Giersig, P. Mulvaney, *J. Phys. Chem. B* 105 (2001) 8810–8815.